PHOTONICS Research

Long range dynamic displacement: precision PGC with sub-nanometer resolution in an LWSM interferometer

Yisi Dong,[1,2] Peng-Cheng Hu,[1,2,*] Haijin Fu,[1,2] Hongxing Yang,[1,2] Ruitao Yang,[1,2] and Jiubin Tan[1,2]

[1]Center of Ultra-precision Optoelectronic Instrument, Harbin Institute of Technology, Harbin 150080, China
[2]Key Laboratory of Ultra-precision Intelligent Instrumentation (Harbin Institute of Technology), Ministry of Industry and Information Technology, Harbin 150080, China
*Corresponding author: hupc@hit.edu.cn

Received 31 August 2021; revised 25 October 2021; accepted 2 November 2021; posted 2 November 2021 (Doc. ID 442057); published 13 December 2021

We propose a precision phase-generated-carrier (PGC) demodulation method with sub-nanometer resolution that avoids nonlinear errors in a laser wavelength sinusoidal modulation fiber-optic interferometer for long range dynamic displacement sensing. Using orthogonal detection and an AC-DC component extraction scheme, the PGC carrier phase delay (CPD) and laser intensity modulation phase delay can be obtained simultaneously to eliminate the nonlinear error from accompanied optical intensity modulation and CPD. Further, to realize long range displacement sensing, PGC phase modulation depth (PMD), determined by the laser wavelength modulation amplitude and the working distance of the interferometer, is required to maintain an optimal value during measurement, including initial position and dynamic movement. By combining frequency sweeping interference and modified PGC-arctan demodulation to measure real-time working distance, adaptive PMD technology is realized based on proportion control. We construct a fiber-optic Michelson and SIOS commercial interferometer for comparison and perform experiments to verify the feasibility of the proposed method. Experimental results demonstrate that an interferometer with sub-nanometer resolution and nanometer precision over a large range of 400 mm can be realized.

https://doi.org/10.1364/PRJ.442057

1. INTRODUCTION

Recently, fiber laser interferometry technology has undergone rapid development. Unlike the traditional interference system based on a discrete mirror group, the fiber-optic interference system has the advantages of compact structure, convenient adjustment of optical path, anti-corrosive properties, and suitability for measurements in extreme environments, hence meeting the high stability and precision embedded measurement requirements [1,2].

There are two kinds of fiber-optic interferometers. One has a fiber-optic coupler [3,4], with its measurement and reference arms in two fibers. This setup is sensitive to external environment factors, such as temperature and stress, making it difficult to achieve high-precision measurements. The other is the micro structure [5], which comprises an optical fiber collimator and spectroscope that can achieve high-precision measurement and is considered as the main research hotspot.

Demodulation technology largely determines the performance of fiber-optic displacement measurement. Based on broadband light sources, a white light interferometer can realize cavity length measurement with sub-nanometer resolution [6]. Although this technology is mature, it is used only for quasi-static measurement and cannot meet the requirement of dynamic measurement. To realize fast signal demodulation, quadrature point intensity demodulation is widely used [7,8], but its dynamic range is limited ($\lambda/4$). In addition to the above demodulation, phase-generated-carrier (PGC) technology is a popular means due to its high sensitivity, high dynamic range, and good linearity [9,10].

PGC technology requires a high-frequency carrier phase signal, which is generated by modulating the laser wavelength and combining the idle length of the interferometer. This is referred to as a laser wavelength sinusoidal modulation (LWSM) fiber-optic interferometer. However, for this interferometer, the carrier phase delay (CPD), accompanied optical intensity modulation (AOIM), and phase modulation depth (PMD) in PGC demodulation can lead to large errors and even fail to demodulate, which severely restricts the displacement measurement accuracy.

Numerous CPD compensation methods [11,12] have been proposed without the consideration of AOIM. Although they

were experimentally verified, none of them can be applied to phase delay compensation in PGC demodulation units affected by AOIM. Researchers from Tianjin University [13] proposed to eliminate AOIM by double photoelectric detection and division operation; however, the double channel synchronization is difficult to realize due to different fiber paths that may induce errors, especially when the modulation frequency reaches the MHz region [14]. To realize accurate double channel synchronization, the fiber delay chain is used, but it is suitable only for short-term measurement in a stable environment due to the instability of two channels.

For PMD control, researchers at St. Petersburg National University [15] used the first four harmonics of the interference signal to realize the stability of PMD. However, the system does not function normally when the phase to be measured is in $n\pi/2$, or when $J_2(C) = 0$ or $J_3(C) = 0$ at some position. Xie *et al.* proposed an active PMD control in PGC demodulation [16] that does not require changes in the modulation amplitude. However, the method needs calculation of four pairs of quadrature harmonic components, which makes the scheme complicated and resource consuming. To reduce resource consumption [17], calculation with three new harmonic components is proposed.

The above two systems function normally when the phase to be measured is in $n\pi/2$, whereas at the position $J_2(C) = 0$ or $J_3(C) = 0$, for large displacement sensing, they fail.

In addition to the above methods, a classical ellipse fitting method [18] simultaneously deals with the effects of three parameters. However, pre-obtained data are necessary for ellipse fitting. Ellipse fitting with combined sinusoidal and triangular modulation [19] was used to obtain pre-data. However, for the LWSM fiber-optic interferometer, the Lissajous diagram of the system is a straight line in numerous cases, such that the above ellipse fitting method cannot be used.

In this study, to solve the above problems and realize precision PGC demodulation in the LWSM fiber-optic interferometer, orthogonal detection and an AC-DC component extraction scheme are used to obtain the CPD and laser intensity modulation phase delay (LIMPD) simultaneously, which uses single channel detection to avoid the asynchronous problem of double channel detection. AOIM and CPD can be effectively eliminated at the same time. By combining frequency sweeping interference and modified PGC-arctan demodulation to measure real-time working distance, the PMD adaptive method is realized based on proportion control, which works including all initial positions and dynamic movements under the normal working distance of the sensing probe and requires less memory resources.

In Section 2, the influence of CPD, AOIM, and PMD in PGC demodulation is analyzed, and a novel precision PGC demodulation is described in detail. The experimental setup and verified experiments are given in Section 3.

2. PRINCIPLE AND METHOD

A. Effects of AOIM and CPD in PGC Demodulation

In the LWSM fiber-optic interferometer, the optical path difference of the interferometer is modulated, and the interference signal that carries the information of the measured displacement is

$$S(t) = kI_0\{1 + m\cos[\omega_0(t-\tau) + \varphi_m]\} \cdot \{1 + v\cos[C\cos\omega_0(t-\tau) + \varphi(t)]\}, \quad (1)$$

where k is the intensity/voltage conversion coefficient; I_0 is the intensity; ω_0 is the angular frequency of the carrier; v is the visibility of the interference signal; $\varphi(t)$ consists of the initial phase and the phase shift caused by the measured displacement; m is the laser intensity modulation coefficient (LIMC), i.e., depth of AOIM, $m = (I_{\max} - I_{\min})/(I_{\max} + I_{\min})$, with $I_{\max}$ and $I_{\min}$ denoting the maximum and minimum output intensities, respectively; φ_m is the LIMPD, i.e., the phase difference between central optical-frequency modulation (COFM) and AOIM in the interference model; and C represents the PMD, whose expression is as follows:

$$C = \frac{4\pi nL}{c}d = \frac{4\pi nL}{c}K_{\mathrm{DL}}i_m, \quad (2)$$

where c is the speed of light in a vacuum, n is air refractive index, d is the modulation depth of laser wavelength (frequency), K_{DL} is the conversion coefficient between laser current and output wavelength, i_m is the amplitude of laser modulation current, and L is the difference between the length of the interferometer measuring arm and the reference arm.

According to the traditional PGC-arctan demodulation algorithm, the interference signal is multiplied by the fundamental frequency carrier $\cos(\omega_0 t)$ and second frequency carrier $\cos(2\omega_0 t)$, and passes through a low-pass filter (LPF) to obtain the following signals:

$$S_1(t) = -kI_0 v\sqrt{a_1^2 + b_1^2} \cdot \{\sin[\varphi(t) - \theta_1]\} + mkI_0\cos\varphi_m/2, \quad (3)$$

$$S_2(t) = -kI_0 v\sqrt{a_2^2 + b_2^2} \cdot \{\cos[\varphi(t) - \theta_2]\}, \quad (4)$$

$$\tan\theta_1 = 2a_1/b_1, \quad (5)$$

$$\tan\theta_2 = 2a_2/b_2, \quad (6)$$

where a_1, a_2, b_1, and b_2 are respectively expressed as

$$a_1 = (m/2)\cdot[J_0(C)\cos(\varphi_c - \varphi_m) - J_2(C)\cos(\varphi_c + \varphi_m)], \quad (7)$$

$$a_2 = (m/2)\cdot[J_3(C)\cos(2\varphi_c + \varphi_m) - J_1(C)\cos(2\varphi_c - \varphi_m)], \quad (8)$$

$$b_1 = J_1(C)\cos\varphi_c, \quad (9)$$

$$b_2 = J_2(C)\cos(2\varphi_c). \quad (10)$$

After the division and arctangent operations, the demodulated signal is described as

$$\varphi(t) + \varphi_{\mathrm{error}}(t) = \varphi'(t) = \arctan[S_1(t)/S_2(t)]. \quad (11)$$

Accordingly, the CPD and AOIM can turn ideal orthogonal signals into non-orthogonal signals, which are unequal in amplitude and have DC bias. Therefore, periodic nonlinear errors $\varphi_{\mathrm{error}}(t)$ can be generated, which severely affect the accuracy of

demodulation and even cause demodulation failure in some cases.

Subsequently, comparative simulation experiments were performed. The CPD was assumed to be from zero to 2π, and the measured phase varied from zero to $\pi/4$ (1/8 interference fringes) at a constant velocity. The PMD was set to $C = 2.63$. The LIMC was set to $m = 0$, $m = 0.2$, and $m = 0.4$. The LIMPD was set to 0, $\pi/2$, and $3\pi/2$. The correct phase demodulation value must be $\pi/4$, and the actual demodulation values are shown in Fig. 1 under different parameter variables. The differences between them are demodulation errors, which also are known as nonlinear errors. CPD and AOIM jointly affect the demodulation of PGC, thus producing nonlinear errors.

B. Effects of PGC PMD Deviation in Long Displacement Sensing

In the above simulation, the PMD is set to a fixed ideal value. If the effects of CPD and AOIM are ignored, the PGC-arctan demodulation scheme will work correctly when the ratio of the first and second order Bessel functions $J_1(C)/J_2(C)$ equals one, i.e., Bessel functions of the first and second orders are equal to each other $J_1(C) = J_2(C)$ and, therefore, do not influence the output signal amplitude. In this case, the output signal from the PGC-arctan demodulation scheme becomes stable, and $C = 2.63$ rad is the optimal PMD value, ensuring proper function of the considered demodulation scheme.

However, when the PMD deviates from the ideal value, the demodulation results are severely affected, and nonlinear errors occur. This problem is particularly serious in the LWSM fiber-optic interferometer, as in the actual displacement sensing, it is difficult to accurately obtain the initial working distance and determine the initial PGC PMD value, which is determined by the working distance and laser wavelength modulation amplitude. Furthermore, in the process of object displacement, the working distance of the system will inevitably change, which has little impact on the displacement at the micrometer level but a significant influence on the displacement at the centimeter level; therefore, the PMD will have large deviations, making the system abnormal. Figure 2 shows the effects of the working distance and laser frequency modulation amplitude in PGC demodulation on the demodulation phase.

As in Fig. 1, the correct phase demodulation value must be $\pi/4$, and the actual demodulation values are shown in Fig. 2. Under different working distances and laser frequency modulation amplitudes, the differences between them are demodulation errors, also known as nonlinear errors. The stability control of PMD is particularly important to realize precise PGC demodulation.

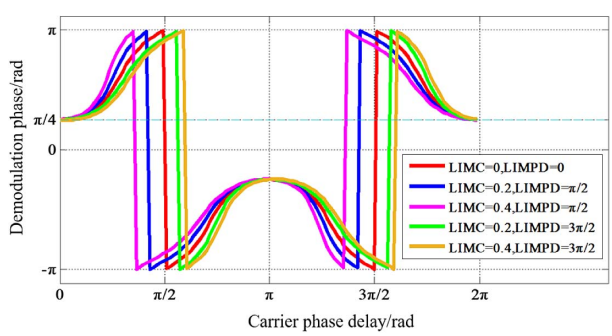

Fig. 1. Effects of CPD, LIMC, and LIMPD on demodulation phase in PGC demodulation.

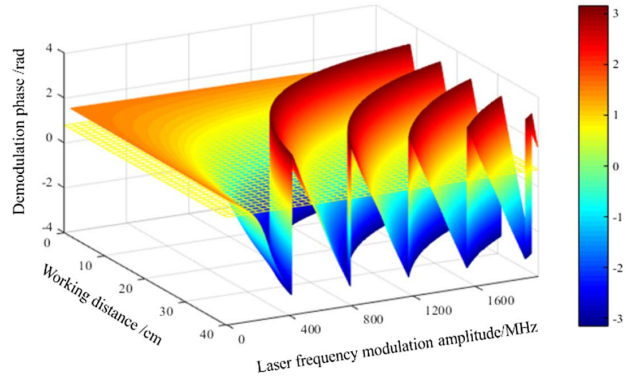

Fig. 2. Demodulation phase on both working distance and laser frequency modulation amplitude.

C. Precision PGC Demodulation for Long Displacement Sensing

As mentioned above, CPD, AOIM, and PMD deviations significantly affect the accuracy of the demodulation results in PGC. Therefore, it is necessary to eliminate the associated errors. The precision PGC demodulation for long displacement sensing includes three steps: (1) calculation and elimination of CPD and LIMPD; (2) initial PMD adaptive technology under different working distances; and (3) dynamic PMD tracing and AOIM elimination for long displacement sensing. A schematic of precision PGC demodulation for long range dynamic displacement in the LWSM interferometer is shown in Fig. 3.

1. Calculation and Elimination of CPD and LIMPD

The objective of this part is to calculate and eliminate CPD and LIMPD. The details are given below.

Step 1: The PMD is set such that the Bessel function coefficients satisfy the equation $J_0 + J_2 = 0$, and $J_n(C)$ is the Bessel function of the first type with order n.

Step 2: The orthogonal detection method is used to recover $S_1(t)$ and $S_2(t)$:

$$\begin{aligned} S_1(t) &= [S(t) \cdot \sin(\omega_0 t)] * h_{\mathrm{LPF}}(t) \\ &= \sin\varphi_c[mkI_0 vJ_0 \cos\varphi(t) - kI_0 vJ_1 \sin\varphi(t)] \\ &\quad + (1/2) \cdot mkI_0 \sin(\varphi_c - \varphi_m), \end{aligned} \tag{12}$$

$$\begin{aligned} S_2(t) &= [S(t) \cdot \cos(\omega_0 t)] * h_{\mathrm{LPF}}(t) \\ &= \cos\varphi_c[mkI_0 vJ_0 \cos\varphi(t) - kI_0 vJ_1 \sin\varphi(t)] \\ &\quad + (1/2) \cdot mkI_0 \cos(\varphi_c - \varphi_m), \end{aligned} \tag{13}$$

where "*" represents convolution, and $h_{\mathrm{LPF}}(t)$ is the impulse response function of the LFP in the time domain, whose cutoff frequency is set to eliminate the frequencies above $w_c/2$.

Step 3: Based on peak value detection (PVD), the DC terms $S_{1\mathrm{DC}}$ and $S_{2\mathrm{DC}}$, and AC terms $S_{1\mathrm{AC}}(t)$ and $S_{2\mathrm{AC}}(t)$ of the $S_1(t)$ and $S_2(t)$ are extracted:

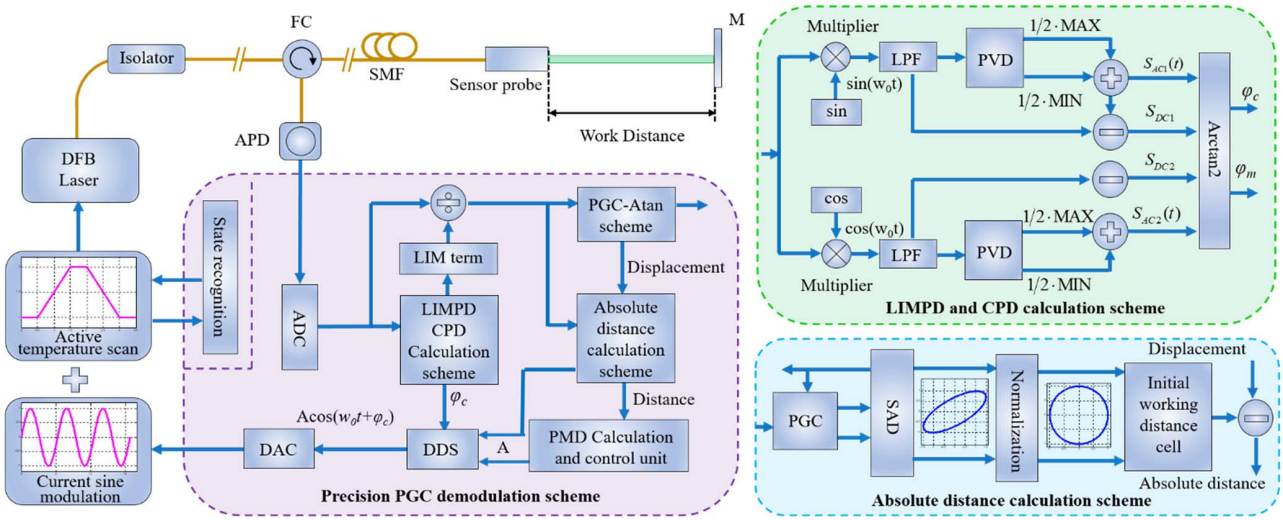

Fig. 3. Schematic of precision PGC demodulation in LWSM interferometer. M, reflector; APD, avalanche photodetector; SMF, single mode fiber; FC, fiber-optic circulator; DDS, direct digital synthesizer; ADC, analog-to-digital converter; LPF, low-pass filter; DAC, digital-to-analog converter; DFB, distributed feedback laser; EN, enabling end of a nonlinearity correction unit; PVD, peak value detection; SAD, signal amplitude detection.

$$S_{\mathrm{DC}} = 1/2\{\mathrm{MAX}[S(t)] + \mathrm{MIN}[S(t)]\}, \tag{14}$$

$$S_{\mathrm{AC}}(t) = S(t) - S_{\mathrm{DC}}, \tag{15}$$

where MAX[x] is the maximum value of the x function, and MIN[x] is the minimum value of the x function.

Step 4: φ_c and $\varphi_c - \varphi_m$ are calculated by the arctangent calculation according to Eqs. (16) and (17), and φ_m can be obtained by subtracting φ_c from $\varphi_c - \varphi_m$:

$$\varphi_c + 2n_1\pi = \arctan 2(S_{1\mathrm{AC}}(t), S_{2\mathrm{AC}}(t)), \tag{16}$$

$$\varphi_c - \varphi_m + 2n_2\pi = \arctan 2(S_{1\mathrm{DC}}(t), S_{2\mathrm{DC}}(t)), \tag{17}$$

$$\varphi_m + 2n\pi = (\varphi_c + 2n_1\pi) - (\varphi_c - \varphi_m + 2n_2\pi). \tag{18}$$

Here, $\arctan 2(x, y)$ extends the domain of $\arctan(x, y)$ to $[-\pi, +\pi]$. Referring to Eq. (1), the simplest way to eliminate AOIM is to divide the interference signal $S(t)$ by the part of light intensity modulation $S_{\mathrm{power}}(t)$. There are three parameters to be determined, namely, m, τ, and φ_m:

$$S_{\mathrm{power}}(t) = 1 + m\cos[\omega_0(t - \tau) + \varphi_m]. \tag{19}$$

Among them, $m = (I_{\max} - I_{\min})/(I_{\max} + I_{\min})$, with $I_{\max}$ and $I_{\min}$ as the maximum and minimum output intensities, respectively. Hence, m can be easily calculated and determined. However, τ and φ_m are relatively difficult to determine and more important.

2. Initial PMD Adaption at Different Working Distances

The main task in this scheme is to control the initial static PMD of the interferometer, which is to avoid the deviation of the initial PMD from the ideal value due to the uncertain initial working distance.

Step 1: PMD pre-control. The main purpose of this step is to prevent the PMD from approaching several special values, where $J_1(C) = 0$ or $J_2(C) = 0$, and the output signal of the LPF from being seriously attenuated, as these scenarios can cause PGC demodulation and subsequent unit failure. The laser wavelength is scanned by increasing the laser drive temperature. In this process, the output of the direct digital synthesizer (DDS) is set to $\cos(\omega_0 t)$. The laser wavelength modulation amplitude is set to d_1, which satisfies the following formula:

$$d_1 = \frac{2.63 \cdot c}{4\pi n L_{\max}}, \tag{20}$$

where $L_{\max}$ is the maximum working distance of the interferometer, which depends on the characteristics of the sensing probe. In this study, the maximum working distance is set to 40 cm. The interference signal, whose AOIM and CPD have been eliminated, is multiplied by $\cos(\omega_0 t)$ and then passes through the LPF to obtain the signal. Next, the obtained signal and above interference signal are sent to the signal amplitude detection (SAD) unit for the following algorithm calculation. The SAD module contains three parts.

Part 1. The AC amplitudes of the interference signal and the obtained signal were extracted by the extremum method and recorded as A and B, respectively.

Part 2. Calculate the value of B divided by $0.4624 \times A$ and record it as H. If $H < 0.5$, proceed to the contents of the third step. If $H \geq 0.5$, keep the current parameters, and end all procedures of SAD.

Part 3. Change the laser frequency modulation amplitude to twice the previous time. The laser wavelength is scanned and the procedure in the first step is repeated. The core concept of the SAD module is as follows: by determining the signal amplitude of the filter output, the laser frequency modulation amplitude can be actively adjusted, and several cycles can be carried out, such that the signal quality corresponding to the adjusted PMD can meet the subsequent processing requirements. After the SAD unit is preprocessed, the signal quality is better at longer working distances. The PMD pre-control is completed after the algorithm described above.

Step 2: PMD precise control. The main purpose of this step is to control the PMD of the system to the optimal value. By increasing the laser drive temperature, the laser wavelength is scanned from λ_1 to λ_2. Meanwhile, the PGC-arctan method is employed. Two signals from LPFs are obtained, as shown by

$$S_1^*(t) = [S^*(t) \cdot \cos(\omega_0 t)] * h_{\mathrm{LPF}}(t) = -kI_0 v J_1(C) \sin \varphi(t), \tag{21}$$

$$\begin{aligned} S_2^*(t) &= [S^*(t) \cdot \cos(2\omega_0 t)] * h_{\mathrm{LPF}}(t) \\ &= -kI_0 v J_2(C) \cos \varphi(t). \end{aligned} \tag{22}$$

However, because the PMD at this time is still not an optimal value, $J_1(C) \neq J_2(C)$, i.e., signal demodulation is still affected by residual nonlinear errors. To obtain demodulation results without nonlinear errors, normalization is used to process two signals from LPFs. The phase change value $\Delta\varphi_0$ is obtained. According to the obtained $\Delta\varphi_0$ and the known λ_1 and λ_2, the initial working distance ΔX of the fiber-optic LWSM interferometer can be obtained through calculation. The calculation formula is as follows:

$$\Delta X = \frac{\lambda^2 \Delta\varphi_{\lambda_1 - \lambda_2}}{4\pi \cdot \Delta\lambda}, \tag{23}$$

where $\Delta\lambda$ is the difference between wavelength λ_1 and wavelength λ_2, and λ is approximately equal to λ_1. Using the obtained true initial interferometer working distance, the ideal laser wavelength modulation amplitude can be set according to Eq. (2) to obtain the ideal PMD.

In summary, by employing the above techniques, the PMD is automatically adjusted to the optimal value. Combined with the elimination of the CPD and AOIM, the nonlinear error is eliminated, and precise PGC demodulation is realized.

3. Dynamic PMD Tracing and AOIM Elimination for Long Displacement Sensing

Above, we described the technique when the object moves statically or in a very small range. However, when the object moves a few tens of centimeters, the PMD will inevitably deviate from the ideal value owing to the change in the working distance of the interferometer. Therefore, the laser wavelength modulation amplitude must be adjusted in real time to realize tracking of the ideal PMD. AOIM will change simultaneously. Thus, dynamic PMD tracing and AOIM elimination for long displacement sensing are necessary. In the movement process of the object to be measured, the real-time working distance can be calculated by subtracting the initial working distance from the displacement value of the object to be measured, after which the real-time PMD C_{new} can be calculated by Eq. (2) and controlled to the ideal value.

For the elimination of dynamic AOIM, according to the experimental records, LIMC is found to change, whereas LIMPD remains unchanged, such that the relationship between LIMC and laser frequency modulation amplitude measured in advance is derived as follows:

$$m(t) = \frac{I_{\max}(t) - I_{\min}(t)}{I_{\max}(t) + I_{\min}(t)} = \frac{k\Delta f(t)}{2I_1}, \tag{24}$$

where I_1 is the output intensity when the laser is not modulated, hence constant. $\Delta f(t)$ denotes the laser wavelength modulation amplitude in real time, and k is the linear coefficient of the optical power variation and the laser frequency modulation amplitude, which can be measured by experiments. Because $\Delta f(t)$ is known, m can be realized according to the formula that likewise follows the real-time change, and dynamic PMD tracing and AOIM elimination for long displacement sensing are realized.

3. EXPERIMENTAL RESULT

The experimental setup of the fiber-optic LWSM interferometer is built. The laser source was a distributed feedback (DFB) laser (DFB PRO BFY, Toptica, Germany), and the interference signal was detected by a photodetector. Interference signal processing and modulation signal generation were performed by a signal-processing board. Using the above devices, we constructed the interferometer proposed in this study. The interferometer used for comparison was SIOS. The measured nanometer displacement was provided by a nanoposition stage (P-733, Physik Instrument, Germany) with a movement range of 30 μm. The measured large range displacement was provided by a stage (A-123.750A1, Physik Instrument, Germany) with a movement range of 750 mm. The experimental setups used for interferometer tests are shown in Fig. 4.

A. Feasibility Verification of Proposed Method

To demonstrate the principle of the proposed method, the experimental proof was carried out.

1. Feasibility Verification of CPD and LIMPD Calculation

In this experiment, the performance of the designed signal processing was evaluated with a simulative interference signal generated by field programmable gate array (FPGA) according to Eq. (1). All simulative parameters can be set flexibly in the FPGA. To prove the effectiveness of the calculation unit of CPD and LIMPD, m, φ_m, φ_c were set to 0.1, $\pi/2$, $5\pi/6$, respectively, and $\varphi(t)$ was changed from zero to $5 \times 2\pi$ rad, corresponding to five interference signal cycles. In practice, in an interference system, this is realized by laser wavelength scanning.

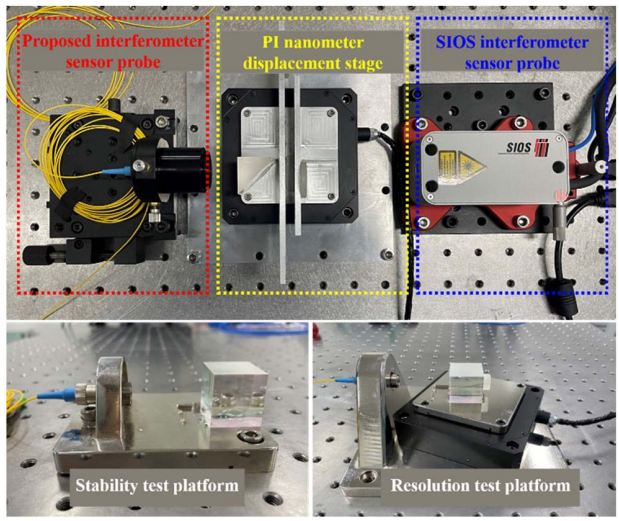

Fig. 4. Experimental setups used for interferometer tests.

Using the CPD and LIMPD calculation method described in Section 2, the AC terms $S_{1AC}(t)$, $S_{2AC}(t)$ of two output signals from filters and the results of the CPD and LIMPD calculation are plotted in Fig. 5.

Figure 5 shows the calculated CPD and LIMPD that are equal to $\pi/2$ and $5\pi/6$, respectively. Thus, the calculated and set delays are the same, and the peak-to-peak value of the noise is lower than 0.015°. Thus, the results of this experiment prove that the developed module is effective.

2. Feasibility Verification of PMD Adaptation for Initial Position and Dynamic Movement

In this part, according to the correlation formula in Refs. [15,16], their schemes were reproduced and compared with the method proposed in this paper. The discussion and analysis of phenomena were also carried out.

First, the initial working distance of the interferometer was set from 2.4 to 40 cm to demonstrate the effectiveness of initial PMD control. The default initial laser frequency modulation amplitude was set to $a = 2.63 \times c/4\pi nL$.

Hence, when the working distance is 5 cm, the corresponding PMD is an ideal value of 2.63. The previous research method [15] and the proposed method were used to initialize the PMD of the system under different working distances. The initial PMD results are plotted in Fig. 6(a). By comparison, the method proposed in this paper can achieve a better initial PMD setting under different working distances with an uncertainty of 0.01 rad. In the previous study, the initial PMD was set incorrectly at some working distances because the Bessel coefficient, the denominator in the calculation formula, would be zero at some working distances, and jump singularities would be generated.

Subsequently, to compare and demonstrate the dynamic control performance of PMD for micro displacement, we set two interference signal cycles of the object, and PMD was calculated and controlled by the previous research method and the one proposed in this study.

The calculated results are plotted in Fig. 6(b), and they show that the calculation and control of PMD in previous research are incorrect when the phase is $n\pi/4$, while the method proposed in this study provides correct results. When the phase is $n\pi/4$, the denominator in the calculation formula was zero, and jump singularities are generated. Although researchers proposed a novel approach [16] to solve this problem, it uses an active control approach that does not change the frequency modulation amplitude but nevertheless leads to errors over a wide range of motions.

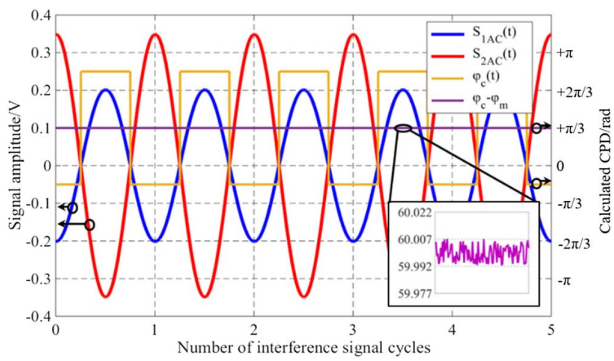

Fig. 5. CPD and LIMPD calculation results: blue traces and red traces correspond to the left ordinate; yellow traces and pink traces correspond to the right ordinate.

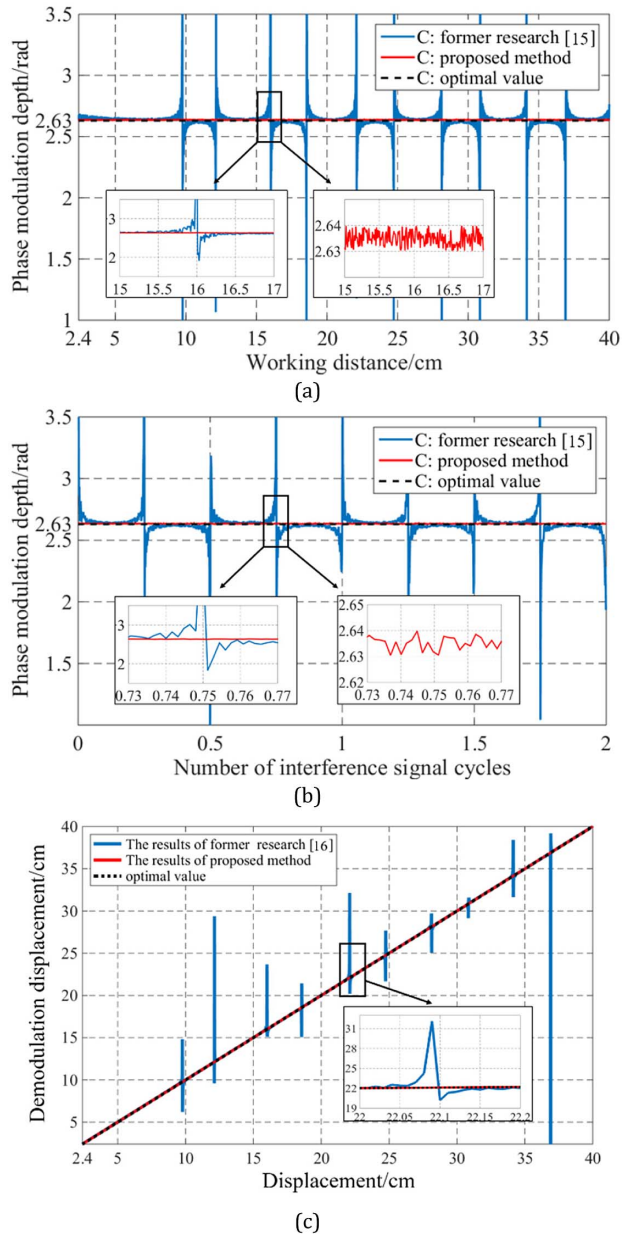

Fig. 6. (a) Phase modulation depth measured by two methods at different working distances. (b) PMD measured by two methods at interferometer operating point. (c) Demodulation results of two methods from 2.4 to 40 cm displacement.

Finally, to show the control performance of PMD in a large range of motions, the object was moved from 2.4 to 40 cm, and the measured demodulation results are drawn in the Fig. 6(c). The proposed method effectively controls the PMD of displacement in a large range of motion. However, the approach yields incorrect results at some distances.

Discussion and analysis of phenomena: in Ref. [15], the combination of the first to fourth harmonics of the input signal

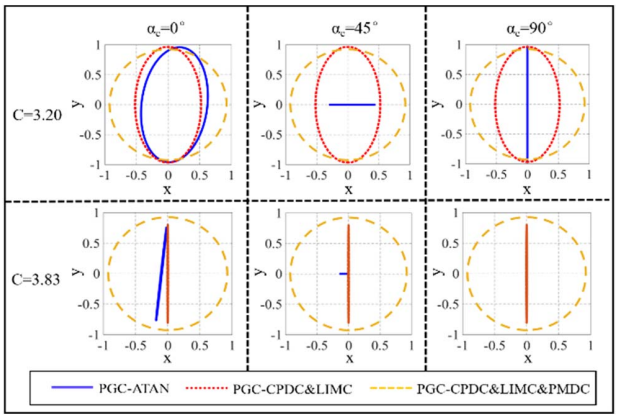

Fig. 7. Lissajous diagrams for three methods under different phase delays and phase modulation depths.

from the optical fiber interferometer was used to obtain PMD. The proportion integral differential (PID) algorithm was used to control the PMD. The core formula is given as follows:

$$\frac{S_2(t)S_3(t)}{[S_3(t)-S_1(t)][S_4(t)-S_2(t)]} = \frac{J_2(C)J_3(C)\sin\varphi(t)\cos\varphi(t)}{(24/C^2)\cdot J_2(C)J_3(C)\sin\varphi(t)\cos\varphi(t)} = \frac{C^2}{24}. \quad (25)$$

When $\varphi(t)$ is $n\pi/2$, or when $J_2(C)=0$ or $J_3(C)=0$, the denominator of Eq. (25) is zero, and the system fails to work properly. Because the initial working distance is uncertain, the above situation is inevitable. Therefore, in some cases, the above method is not applicable. In Ref. [16], instead of calculating PMD, the phase to be measured is directly obtained by Eq. (26), so the system functions normally when the phase to be measured is in $n\pi/2$, whereas when $J_2(C)=0$ or $J_3(C)=0$, they fail. As for Ref. [17], it can be seen that it is similar to the above method:

$$\varphi(t) = \frac{T_y}{T_x} = \frac{A\sqrt{3J_2(C)J_3(C)/C}\cdot\sin\varphi(t)}{A\sqrt{3J_2(C)J_3(C)/C}\cdot\cos\varphi(t)}. \quad (26)$$

The above analysis and discussion are in good agreement with the experimental results. It proves that the method in this paper can work including all initial positions and dynamic movements and avoids the production of jump singularities.

3. Feasibility Verification of Modified PGC Proposed in This Paper

The above experiments verify the proposed method of CPD and LIMPD simultaneous calculation and PMD control method for initial position and dynamic movement of an object. Subsequently, two demodulation algorithms of PGC-CPDC–LIMC and PGC-CPDC–LIMC–PMDC composed of the above technologies were verified by experiments.

First, the CPD was set as 0°, 45°, and 90°, and the PMD was set as 3.20 and 3.83; in total, there were six combinations. Using PGC-arctan (ATAN) and the above two algorithms for signal processing, the Lissajous diagrams of the signals obtained by the two filters are drawn in Fig. 7.

When PMD is 3.20, CPD is zero, and the Lissajous diagrams of PGC-ATAN and PGC-CPDC–LIMC are both elliptical. When CPD is $\pi/4$ or $\pi/2$, PGC-ATAN is close to a straight line, and the Lissajous diagram of PGC-CPDC–LIMC will not be affected. However, when the PMD is 3.83, the Lissajous diagrams of PGC-ATAN and PGC-CPDC–LIMC both show straight lines, which means that the normal demodulation cannot be performed. Simultaneously, the Lissajous diagram of the demodulation result obtained by PGC-CPDC–LIMC–PMDC is consistently a circle, such that demodulation without nonlinear errors can be carried out.

The classical ellipse fitting nonlinear elimination method was employed to further compare system performance. The CPD was set to 20° and 40°, m was set to 0.1, and PMD changed from 1.43 to 3.83 rad with a step of 0.3 rad. signal to noise and distortion ratio (SINAD) values of each method were calculated and plotted. As shown in Fig. 8, the PGC-ATAN method is consistently affected by CPD, LIMC, and PMD, which reduces the SINAD value significantly. The SINAD value of the PGC-CPDC–LIMC method improves when $C=2.63$; however, with the change in C, it decays with the axis of 2.63.

In contrast, the SINADs of ellipse fitting and PGC-CPDC–LIMC–PMDC are consistently better. However, when C is

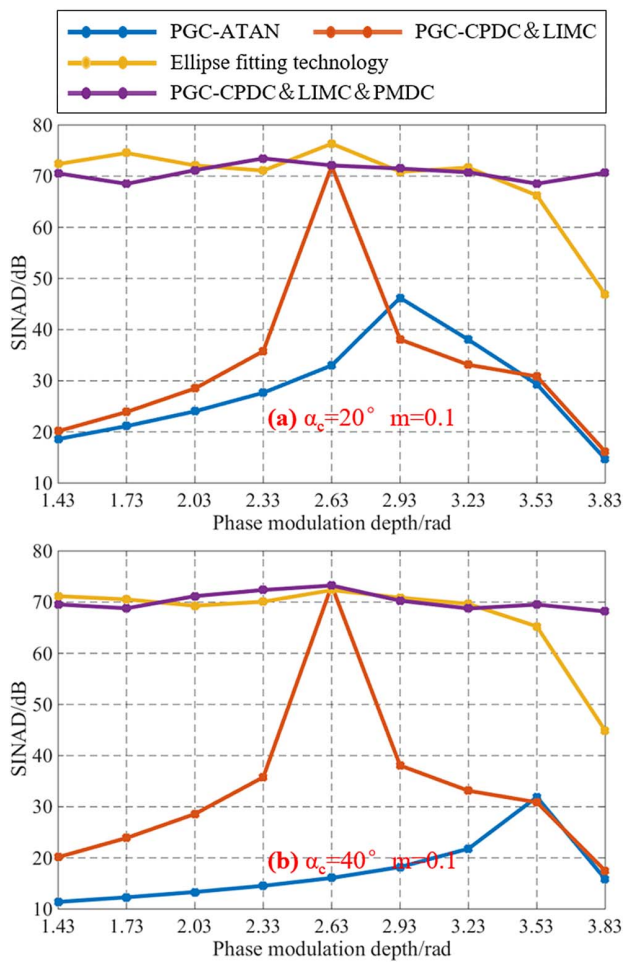

Fig. 8. SINAD values for four methods under different phase delays and phase modulation depths.

close to 3.83, the SINAD of ellipse fitting starts to decline. The reason is that the Lissajous diagram is close to a straight line at this time, and hence it is unable to fit the ellipse well. In summary, the effectiveness and superiority of the method proposed in this study are demonstrated by comparative experiments.

B. Displacement Measurement Experiment

1. Feasibility Verification of PMD Adaptation for Initial Position and Dynamic Movement

First, the small range displacement was tested and compared. The nanometer displacement stage was set to move for 3 μm, and the step was set as 5 nm. The proposed interferometer and SIOS SP-NG were used for the respective tests.

The test results of the displacement stage and the two interferometers are plotted in Fig. 9(a), and the difference between the measured results of the interferometer and the displacement stage is calculated and plotted in Fig. 9(b). The displacement offset is observed at ±1 nm. Simultaneously, the performance of the proposed interferometer is similar to that of the SIOS interferometer.

2. Experiment for a Large-Scale Displacement Measurement

Subsequently, a large-scale displacement test and comparison were carried out. The Physik Instrumente (PI) displacement stage is set to move 400 mm, and the interferometer proposed in this paper and SIOS SP-NG are used for the respective tests.

The test results of the two interferometers and the offset with the displacement stage are plotted in Fig. 10(a). The offsets are found to be similar, which may be caused by the accuracy of the displacement stage. The difference between the measured values of two interferometers is plotted in Fig. 10(b). The displacement difference ranges between −65 and 50 nm.

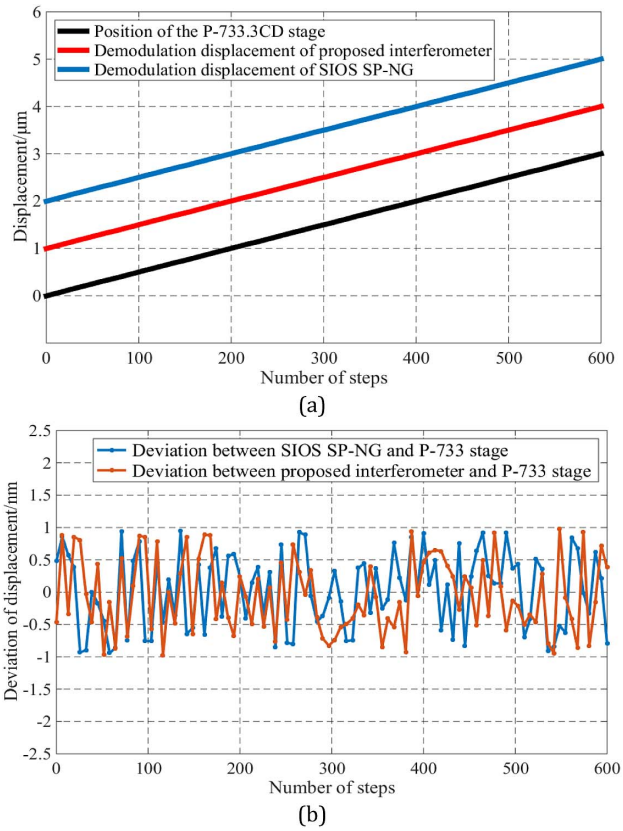

Fig. 9. Experimental results for nanometer displacement measurement with 5 nm step size.

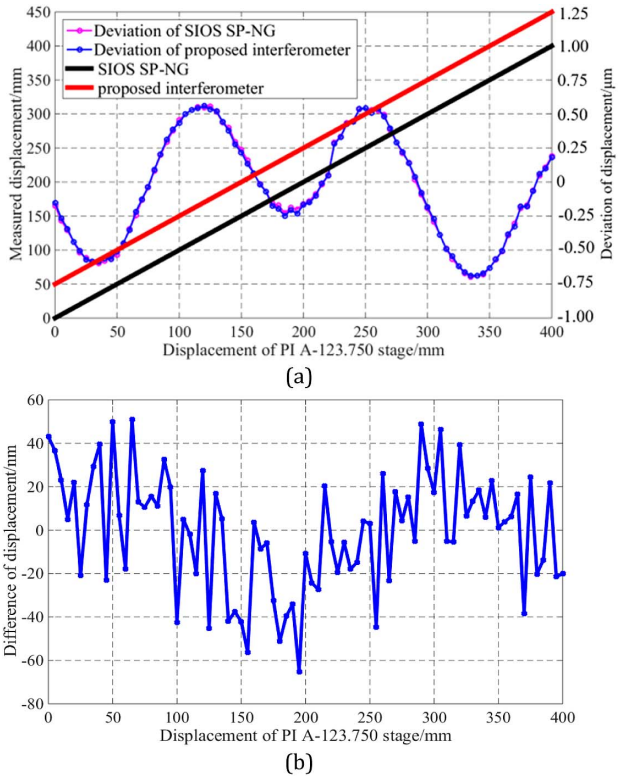

Fig. 10. Comparison experiment of large range displacement measurements.

3. Resolution and Stability of Proposed Interferometer

Next, the resolution of the proposed interferometer was tested, and the nanometer displacement stage parameters were set to a round-trip step of 0.4 nm and a step time of 1 s.

Figure 11(a) shows that there is an obvious round-trip step that can be distinguished; however, because the noise of the displacement stage is superimposed on the signal, better measurement results can be obtained with a more accurate displacement stage. Hence, the resolution of the interferometer proposed in this study is below 0.4 nm.

The stability test platform is made of high-stability material, and the object to be tested is cured by UV glue. The system stability was measured for 1 h. The results are plotted in Fig. 11(b). The drift within 1 h is below 2.5 nm, and the short-term stability in 1 min is below 0.4 nm. Therefore, according to the experimental results, an interferometer with sub-nanometer resolution and nanometer precision can be realized.

4. CONCLUSION

A fiber laser interferometer with sub-nanometer resolution is proposed for use in large-scale measurements. An optimized PGC algorithm is employed in the interferometer. First, a method is proposed to simultaneously calculate CPD and LIMPD, to compensate for and eliminate the influence of CPD and AOIM. Unlike other studies on the elimination

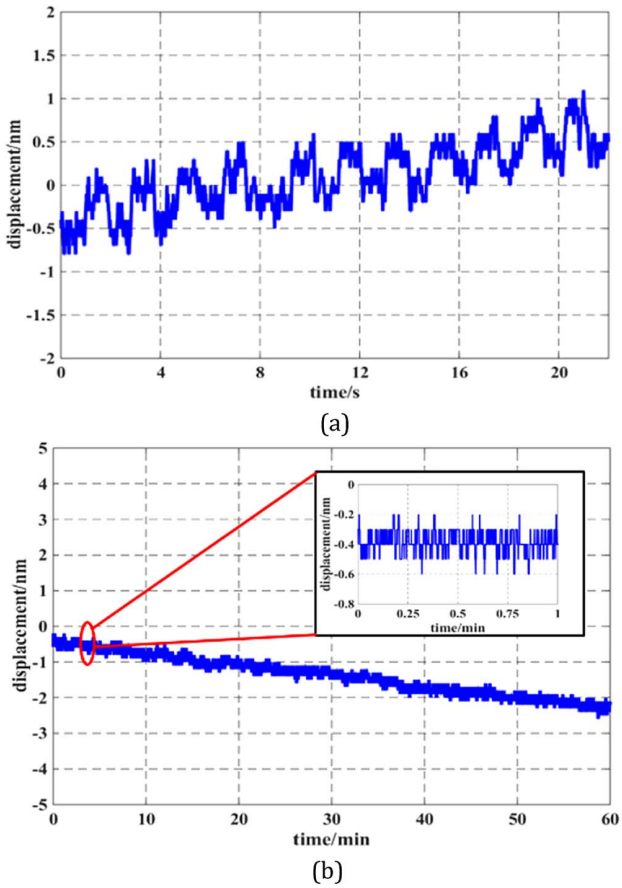

Fig. 11. Experimental results of displacement measurement resolution of proposed interferometer and its long-term stability.

of CPD, AOIM is added to the model, which increased the accuracy of demodulation. Second, we propose a method to control the PMD by combining frequency sweeping interference and modified PGC-arctan demodulation to measure the real-time working distance. Through comparative experiments, the advantages of this method are demonstrated. It can be used for large-scale displacement measurement, and it simultaneously avoids the production of jump singularities with movement as observed with other methods. Therefore, it improves the practicability and demodulation accuracy of the system. Displacement experiments show that the proposed interferometer achieves large range displacement measurements and subnanometer measurement accuracy. In future studies, we plan to correct the idle zone error of the interferometer by combining the obtained initial working distance with the refractive index testing instrument.

Funding. National Natural Science Foundation of China (52061135114); National Major Science and Technology Projects of China (2017ZX02101006-005).

Acknowledgment. Y. D. thanks the National Natural Science Foundation for supporting this work.

Disclosures. The authors declare no conflicts of interest.

Data Availability. Data underlying the results presented in this paper are not publicly available at this time but may be obtained from the authors upon reasonable request.

REFERENCES

1. S. Yin, P. B. Ruffin, and F. T. S. Yu, *Fiber Optic Sensors*, 2nd ed. (CRC University, 2008).
2. E. Udd and W. B. Spillman, eds., *Fiber Optic Sensors: An Introduction for Engineers and Scientists* (Wiley, 2011).
3. J. Song, W. Li, P. Lu, Y. Xu, L. Chen, and X. Bao, "Long-range high spatial resolution distributed temperature and strain sensing based on optical frequency-domain reflectometry," IEEE Photon. J. **6**, 6801408 (2014).
4. D. P. Zhou, Z. Qin, W. Li, L. Chen, and X. Bao, "Distributed vibration sensing with time-resolved optical frequency-domain reflectometry," Opt. Express **20**, 13138–13145 (2012).
5. Y. Dong, P. Hu, M. Ran, H. Fu, H. Yang, and R. Yang, "Correction of nonlinear errors from PGC carrier phase delay and AOIM in fiber-optic interferometers for nanoscale displacement measurement," Opt. Express **23**, 18997–19009 (2020).
6. X. Zhou and Q. Yu, "Wide-range displacement sensor based on fiber-optic Fabry–Perot interferometer for subnanometer measurement," IEEE Sens. J. **11**, 1602–1606 (2011).
7. Q. Wang and Z. Ma, "Feedback-stabilized interrogation technique for optical Fabry–Perot acoustic sensor using a tunable fiber laser," Opt. Laser Technol. **51**, 43–46 (2013).
8. X. Mao, X. Zhou, and Q. Yu, "Stabilizing operation point technique based on the tunable distributed feedback laser for interferometric sensors," Opt. Commun. **361**, 17–20 (2016).
9. A. Dandridge, A. B. Tveten, and T. G. Giallorenzi, "Homodyne demodulation scheme for fiber optic sensors using phase generated carrier," IEEE J. Quantum Electron. **18**, 1647–1653 (1982).
10. T. R. Christian, P. A. Frank, and B. H. Houston, "Real-time analog and digital demodulator for interferometric fiber optic sensors," Proc. SPIE **2191**, 324–336 (1994).
11. S. Zhang, L. Yan, B. Chen, Z. Xu, and J. Xie, "Real-time phase delay compensation of PGC demodulation in sinusoidal phase-modulation interferometer for nanometer displacement measurement," Opt. Express **25**, 472–485 (2017).
12. A. N. Nikitenko, M. Y. Plotnikov, A. V. Volkov, M. V. Mekhrengin, and A. Y. Kireenkov, "PGC-ATAN demodulation scheme with the carrier phase delay compensation for fiber-optic interferometric sensors," IEEE Sens. J. **18**, 1992–1995 (2018).
13. K. Wang, M. Zhang, F. Duan, S. Xie, and Y. Liao, "Measurement of the phase shift between intensity and frequency modulations within DFB-LD and its influences on PGC demodulation in a fiber-optic sensor system," Appl. Opt. **52**, 7194–7199 (2013).
14. Y. Dong, P. Hu, Z. Le, H. Fu, H. Yang, and R. Yang, "Phase modulation depth setting technique of a phase-generated-carrier under AOIM in fiber-optic interferometer with laser frequency modulation," Opt. Express **28**, 31700–31713 (2020).
15. A. V. Volkov, M. Y. Plotnikov, M. V. Mekhrengin, G. P. Miroshnichenko, and A. S. Aleynik, "Phase modulation depth evaluation and correction technique for the PGC demodulation scheme in fiber-optic interferometric sensors," IEEE Sens. J. **17**, 4143–4150 (2017).
16. J. Xie, L. Yan, B. Chen, and Y. Lou, "Extraction of carrier phase delay for nonlinear errors compensation of PGC demodulation in an SPM interferometer," J. Lightwave Technol. **37**, 4143–4150 (2019).
17. L. Yan, Y. Zhang, J. Xie, Y. Lou, B. Chen, S. Zhang, and Y. Zhou, "Nonlinear error compensation of PGC demodulation with the calculation of carrier phase delay and phase modulation depth," J. Lightwave Technol. **39**, 2327–2335 (2021).
18. P. L. M. Heydemann, "Determination and correction of quadrature fringe measurement errors in interferometers," Appl. Opt. **20**, 3382–3384 (1981).
19. L. Yan, Z. Chen, J. Xie, and E. Zhang, "Precision PGC demodulation for homodyne interferometer modulated with a combined sinusoidal and triangular signal," Opt. Express **26**, 4818–4831 (2018).